Qi et al. *NPG Asia Materials* (2018) 10: 385–396
DOI 10.1038/s41427-018-0039-0

NPG Asia Materials

ARTICLE Open Access

The biotransformation of graphene oxide in lung fluids significantly alters its inherent properties and bioactivities toward immune cells

Yu Qi[1], Yun Liu[2,3], Tian Xia[4], An Xu[3], Sijin Liu[2,5] and Wei Chen[1]

Abstract

Engineered nanomaterials (such as graphene oxide, GO) have shown great potential in biomedical applications as therapeutic and imaging agents. However, little is known about their potential transformations in biological settings, which may alter their physicochemical properties and consequently hinder their biomedical applications. Here, we show that GO undergoes a significant physicochemical transformation in two simulated human lung fluids–Gamble's solution and artificial lysosomal fluid (ALF), as the organic acids (e.g., citrate and acetate) in the lung fluids cause the reduction of GO, which is mainly due to the conversion of epoxy and carbonyl groups to phenolic groups. This biotransformation markedly inhibits the endocytosis of GO by scavenging macrophages. Notably, the alterations that occur in Gamble's solution enhance the layer-by-layer aggregation of GO, resulting in the precipitation of GO and a reduction in its interaction with cells, whereas the changes that occur in ALF lead to edge-to-edge aggregation of GO, thereby enhancing the adhesion of large sheet-like GO aggregates on the plasma membrane without cellular uptake. The varied interaction mechanisms with macrophages eventually induce different proinflammatory reactions. Experiments conducted in mice corroborated the morphological alterations of GO in a realistic lung microenvironment. Overall, the findings suggest that the biotransformation of nanomaterials may significantly alter their inherent properties and therefore affect their biosafety, such as the clearance of "worn-out" nanomaterials by immune cells, giving rise to potentially long-term side effects at the accumulation sites.

Introduction

Recent advances in nanotechnology provide unprecedented opportunities to facilitate precision medicine initiatives for both therapeutics and diagnostics[1,2]. Thus, a variety of engineered nanomaterials (e.g., graphene oxide, GO) are intensively researched for various therapeutic and imaging purposes[3–8]. Nonetheless, it is necessary to note that all the current biomedical applications are based on the predesigned physicochemical properties of nanomaterials without considering their potential transformation in biological settings, which may alter their physicochemical properties and consequently hinder their biomedical applications. For instance, biotransformations may influence how nanomaterials interact with the immune cells (e.g., macrophages) responsible for clearing the "worn-out" particles out of the body[9,10]. Thus, understanding the potential transformations and their effects on the ultimate fate of nanomaterials is critical for ensuring the biosafety of nanomaterials.

Correspondence: Sijin Liu (sjliu@rcees.ac.cn) or Wei Chen (chenwei@nankai.edu.cn)
[1]College of Environmental Science and Engineering, Ministry of Education Key Laboratory of Pollution Processes and Environmental Criteria, Tianjin Key Laboratory of Environmental Remediation and Pollution Control, Nankai University, 300350 Tianjin, China
[2]State Key Laboratory of Environmental Chemistry and Ecotoxicology, Research Center for Eco-Environmental Sciences, Chinese Academy of Sciences, 100085 Beijing, China
Full list of author information is available at the end of the article
These authors contributed equally: Yu Qi, Yun Liu.

© The Author(s) 2018
Open Access This article is licensed under a Creative Commons Attribution 4.0 International License, which permits use, sharing, adaptation, distribution and reproduction in any medium or format, as long as you give appropriate credit to the original author(s) and the source, provide a link to the Creative Commons license, and indicate if changes were made. The images or other third party material in this article are included in the article's Creative Commons license, unless indicated otherwise in a credit line to the material. If material is not included in the article's Creative Commons license and your intended use is not permitted by statutory regulation or exceeds the permitted use, you will need to obtain permission directly from the copyright holder. To view a copy of this license, visit http://creativecommons.org/licenses/by/4.0/.

Most nanomaterials predominantly deposit in the lungs after administration either through direct inhalation of a spray or intravenous injection, which depends on the imaging and therapeutic purposes[11,12]. Of note, lung fluids contain an abundance of reactive organic acids and phosphorus, which may induce the oxidation/reduction of nanomaterials. The potential for reaction with these constituents in biological media is particularly relevant for graphene materials (especially GO), as these materials are reactive and prone to reduction, even under relatively mild conditions[13]. To date, little is known about the potential transformation of graphene materials in the lungs and the potential implications for biomedical applications.

The primary objective of this study was to prove that nanomaterials undergo significant biotransformations in lung fluids, which may subsequently compromise their biosafety by impeding their clearance by immune cells. GO was selected as the model nanomaterial due to its versatility in biological applications. Here, we show that the alteration of the GO physicochemical properties in two simulated lung fluids—Gamble's solution and artificial lysosomal fluid (ALF)—greatly hinders its elimination by macrophages via distinctly different mechanisms depending on the specific biological settings involved, which could lead to potentially long-term side effects. Treatment with Gamble's solution simulates the interaction between GO with the interstitial fluid deep within the lung under healthy conditions. The ALF treatment simulates the scenario in which GO sheets are phagocytosed by macrophages, subsequently rereleased into the lung system once the cells are dead, and then participate in subsequent interaction with other macrophages. Two extracellular and intercellular transformation pathways occur simultaneously in the lung. Overall, our findings may have significant implications for the application of nanomaterials in biomedicine, and they highlight the importance of understanding the in vivo biotransformation of nanomaterials.

Materials and methods

Preparation and characterization of GO materials

GO (>99%) was purchased from Nano Materials Tech Co. (China). 1,4-Epoxynaphthalene, 1,4-naphthoquinone, benzoic acid, 2-naphthoic acid, and the inorganic and organic acids and their salts used to prepare the simulated lung fluids were obtained from Sigma-Aldrich (China).

X-ray diffraction (XRD) patterns were recorded using a Rigaku D/Max III diffractometer (Rigaku Inc., Japan) with Cu K radiation, with a wavelength (λ) = 1.5418 Å Fourier transform infrared (FT-IR) transmission spectra were obtained using a 110 Bruker TENSOR 27 apparatus (Bruker Optics Inc., Germany). Raman spectra were recorded with a Renishaw inVia Raman spectrometer (RM2000, Renishaw, UK). The surface elemental compositions were determined by X-ray photoelectron spectroscopy (XPS) (PHI 5000 VersaProbe, Ulvac-PHI, Japan). The physical dimensions of the samples were characterized by scanning electron microscopy (SEM) (FEI Nanosem 430, FEI, USA), transmission electron microscopy (TEM) (JEM-2100, JEOL, Japan), and atomic force microscopy (AFM) (Dimension 3100, DJ08, Veeco, USA).

Transformation of GO in lung fluids

To examine the transformation of GO in two simulated human lung fluids, a 25 μg/mL GO suspension was first prepared in Gamble's solution or ALF (the detailed compositions of these lung fluids are given in Table S1). Next, the suspension was slowly shaken (HWY-2122, China) at 80 rpm and 37 °C for 5 days and then filtered through 0.22-μm membrane filters. The biotransformed GO material that remained on the filter was collected and washed by ultrasonication at 100 W for 30 min. The rinsing procedure was repeated three times to remove extra salts. Afterward, the biotransformed GO was collected by vacuum drying, and a fraction of the material was used for material characterization. Stock solutions (1 μg/mL) of the materials were prepared by sonicating the respective material in a water bath and then stored in borosilicate glass containers at 4 °C in the dark.

The GO transformation experiments involving individual components or an assortment of lung fluid components were carried out according to the same procedures as in the experiments using complete Gamble's solution and ALF. For the reactions of model organic molecules, a stock solution of a model organic molecule (in methanol) was injected into 200 ml of Gamble's solution or an aqueous solution of citrate in pH buffer and then incubated for 5 days. Afterward, the aqueous solution was extracted with dichloromethane, and the reaction products were identified using liquid chromatography–mass spectrometry–mass spectrometry (Waters Xevo TQ-S, USA) with a full scan from *m/z* 80–210 in positive electrospray ionization mode and a dwell time of 400 ms.

Cell culture

Murine macrophage cell line J774A.1 and HEK293 cells were purchased from the Shanghai Cell Bank of Type Culture Collection of China. Cells were cultured in Dulbecco's modified Eagle's medium (DMEM) (Gibco BRL Life Technologies Inc., USA) supplemented with 10% fetal bovine serum (FBS) and 100 units/mL penicillin/streptomycin (Invitrogen) in a humidified 5% CO_2-balanced air incubator at 37 °C. The HEK293 toll-like receptor 4 (TLR4) cell line, originally purchased from InvivoGen Inc. (San Diego, CA, USA), was a kind gift provided by Dr.

Shitao Li at Harvard Medical School. HEK293-TLR4 cells were cultured in DMEM containing 10% FBS, 100 units/mL penicillin G, and 100 μg/mL streptomycin.

Quantitative reverse transcription-polymerase chain reaction (qRT-PCR) assay of gene expression

qRT-PCR analysis was performed to characterize the expression levels of tumor necrosis factor-α (TNF-α) mRNA transcript in this assay. Briefly, cells were cultured in six-well plates and then incubated with 20 μg/mL GO nanomaterials for 12 h. Total RNA was isolated from cells using Trizol (Life Technologies). qRT-PCR analysis of the TNF-α mRNA level was performed using SYBR Green qPCR mix (Promega Inc., USA) on an Mx3005P qRT-PCR instrument (Bio-Rad, USA). The primer sequences for the PCR reactions were as follows: human TNF-α: forward primer: 5′-CAGAGGGCCTGTACCTCATC-3′, reverse primer: 5′-GGAAGACCCCTCCCAGATAG-3′. Human GAPDH (used as the internal control for normalization): forward primer: 5′-GAAGGTGAAGGTCGGAGT-3′, reverse primer: 5′-GAAGATGGTGATGGGATTTC-3′.

Intracellular characterization of GO materials by confocal micro-Raman spectroscopy

Confocal micro-Raman spectroscopy was employed to track the intracellular GO nanomaterials. After treatment with 5 μg/mL GO nanomaterials for 24 h, the cells were gently washed with PBS, fixed with 2.5% glutaraldehyde, and then excited with a 633-nm laser. Raman mapping was completed with a step size of 1 μm and an acquisition time of 3 s under 10% power. The mapping images were obtained by collecting the Raman spectrum at each spot. The Raman map was also merged with its corresponding bright-field morphological image.

Cellular localization of GO nanomaterials through TEM

Cells were seeded in 6-cm plates at a density of 2×10^6 per plate and incubated for 24 h. Cells were exposed to GO nanomaterials at 5 μg/mL and incubated for another 24 h, which was followed by cell collection. The harvested cells were fixed with 2.5% glutaraldehyde solution and embedded in epoxy resin. TEM samples were prepared as previously reported[14]. Areas containing cells were block mounted and cut into ultrathin sections (70 nm). The ultrathin cell specimens were placed on grids, stained with 1% lead citrate and 0.5% uranyl acetate and finally examined. Subcellular localization of the nanomaterials was conducted using a high-resolution JEOL JEM 2010F transmission electron microscope (Hitachi Scientific Instruments, Japan).

Animal experiments

BALB/C male mice (7–8-weeks old, body weight of ~20 g) were purchased from Beijing Vital River Laboratory Animal Technology (Beijing, China). All animal experimental protocols were approved by the Animal Ethics Committee at the Research Center for Eco-Environmental Sciences, Chinese Academy of Sciences. All animals were housed in a specific pathogen-free (SPF grade) and aseptic animal facility. Mice were randomly divided into nine groups with $n = 6$ in each group. Mice were anesthetized by intraperitoneal injection of pentobarbital sodium, and GO or biotransformed GO was then intratracheally instilled into the lungs at a dose of 2.5 mg/kg body weight. The control group received saline only. After 3 h, bronchoalveolar lavage was performed for TEM analysis of the fluid. For the acute single treatment, mice were killed 6 or 24 h post administration, and the lung tissues were immediately collected and fixed in 10% formaldehyde solution in PBS. The fixed lung-tissue specimens were embedded in paraffin and sliced into sections for further hematoxylin–eosin (H&E) staining following the standard protocols.

Determination of inflammatory cytokines

Cells were seeded in 96-well plates overnight and then treated with 20 μg/mL GO nanomaterials for 24 h. Afterward, the cell culture medium of each well was collected and centrifuged. The concentrations of TNF-α and IL-6 released into the cell-culturing supernatants were quantitatively assayed with kits from R&D Systems Inc., USA.

Table 1 Physicochemical properties of pristine and biotransformed GO materials

GO/transformed GO[b]	C[a] (wt%)				Total C[a] (wt%)	Total O[a] (wt%)	C/O ratio	I_D/I_G
	Aromatic rings	Epoxy/hydroxyl	Carbonyl	Carboxyl				
Pristine GO	24.62	33.88	6.02	5.69	70.23	29.03	2.41	0.62
Gamble-GO	29.04	28.61	1.92	8.70	68.27	28.07	2.43	0.85
ALF-GO	22.88	26.19	–	25.91	74.98	23.58	3.18	0.84

[a] Analyzed with X-ray photoelectron spectroscopy
[b] Pristine GO represents untreated GO; Gamble-GO and ALF-GO represent GOs treated with one of the two simulated human lung fluids, Gamble's solution, and artificial lysosomal fluid (ALF)

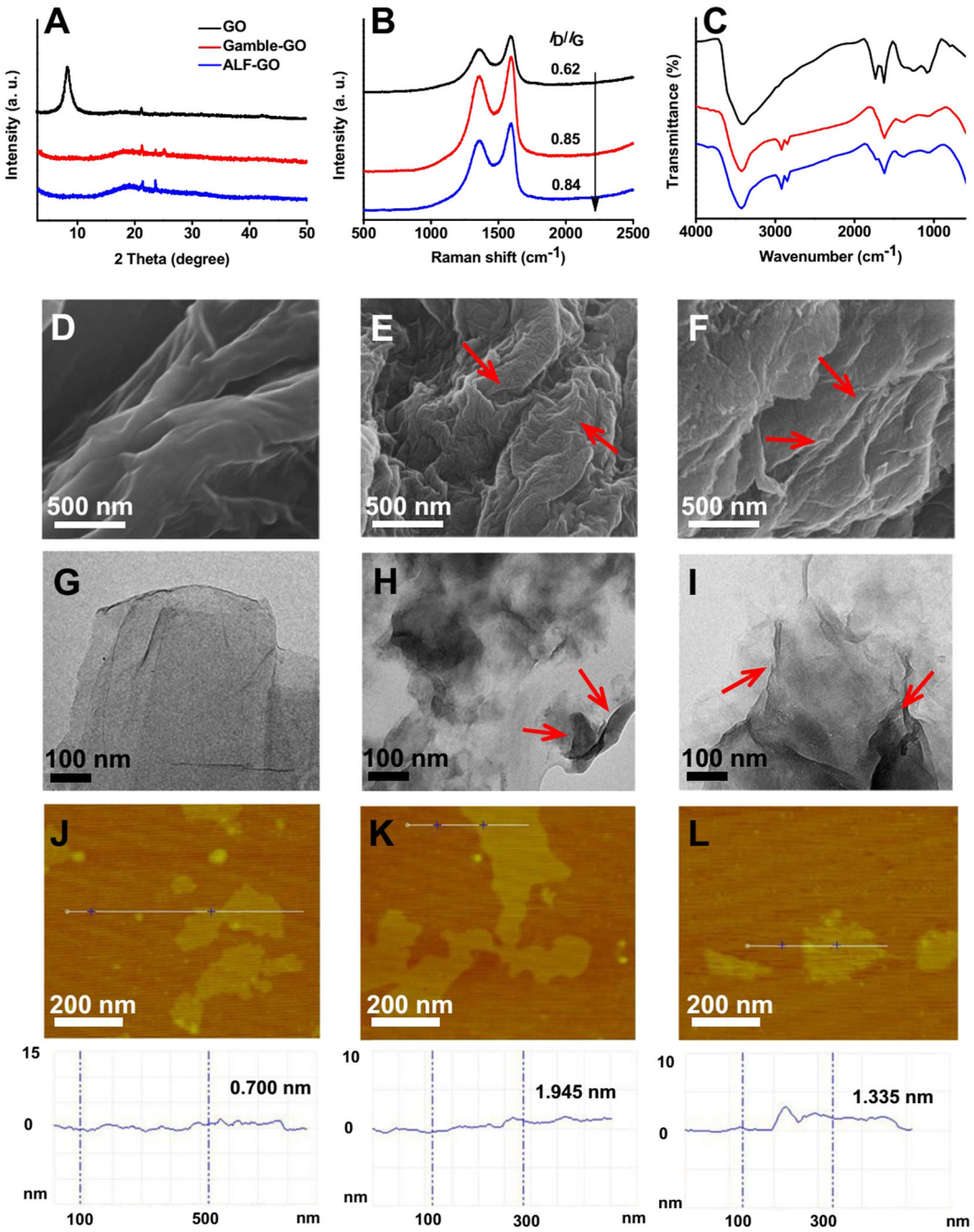

Fig. 1 Physicochemical properties of pristine GO, GO treated with Gamble's solution (Gamble-GO), and GO treated with artificial lysosomal fluid (ALF-GO), showing that significant reduction and morphological changes occurred when GO was treated with simulated human lung fluids. The X-ray diffraction (XRD) patterns (**a**), Raman spectra (**b**), and Fourier transform infrared (FT-IR) transmission spectra (**c**) show the disappearance of the characteristic peak of GO (at ~10°), the loss of surface O-containing functional groups, and the reduction of GO upon biotransformation. The scanning electron microscopy (SEM) and transmission electron microscopy (TEM) images of GO (**d**, **g**), Gamble-GO (**e**, **h**), and ALF-GO (**f**, **i**) show that the surfaces of the biotransformed GOs were more wrinkled than that of pristine GO. The atomic force microscopy (AFM) images of GO (**j**), Gamble-GO (**k**), and ALF-GO (**l**) show that the thickness of the GO nanosheets increased upon biotransformation

Statistical analysis

All data are represented as the mean ± standard deviation. Statistical analysis was performed using an independent *t*-test or a one-way ANOVA test. *P* values less than 0.05 ($P < 0.05$) were considered statistically significant.

Results and discussion

GO undergoes significant physicochemical transformation in lung fluids

To examine the biotransformation of GO materials in the lung, we treated GO with two simulated human lung fluids: Gamble's solution and ALF. The physicochemical properties of GO were substantially altered by incubation in these simulated lung fluids, and between the two treatments, more significant changes were induced by incubation in ALF (the biotransformed GO materials are hereafter referred to as "Gamble-GO" and "ALF-GO"). Treating GO with the simulated human lung fluids resulted in the reduction of GO, as evidenced by an increase in the C/O ratio, particularly for ALF-GO (Table 1). The XRD patterns (Fig. 1a) show that after incubation in the lung fluids, the (002) peak of GO (~10°) disappeared, whereas the intensity of the broad diffraction peak at ~20° increased, corroborating the reduction of GO[15]. The Raman spectra (Fig. 1b) show an increase in the I_D/I_G value following the treatments (Table 1), which is likely attributable to the formation of new graphitic domains with sizes smaller than those of GO before reduction[16,17].

Treating GO with the lung fluids also resulted in significant changes in the concentrations and distributions of the surface O-containing functionalities, as indicated by the FT-IR spectra (Fig. 1c) and the deconvoluted peaks of the C1s XPS spectra that correspond to carbon atoms with different chemical states (Table 1, Figures S1 and S2). For example, pristine GO contained 33.88% C–OH/C–O–C, which is considerably higher than that of Gamble-GO (28.61%) and ALF-GO (26.19%). The decrease in the carbonyl group content was more significant, as it changed from 6.02% for GO to 1.92% for Gamble-GO and was not detectable for ALF-GO. In comparison, the biotransformation of GO resulted in an increase in the content of carboxyl groups from 5.69% for GO to 8.70% for Gamble-GO and 25.91% for ALF-GO. The FT-IR spectra (Fig. 1c) also show the loss of epoxy groups (epoxy C–O group bending band at ~1217 cm^{-1})[18] and a substantial decrease in the content of carbonyl groups (C=O stretching band at ~1670 cm^{-1})[18] upon treatment with the lung fluids, whereas an increase in the hydroxyl group content (O–H bending band at ~1385 cm^{-1})[18] was observed.

The SEM images show that Gamble-GO and ALF-GO were more wrinkled than the untreated GO (Fig. 1). The TEM images of the GO materials in both DI water and DMEM (Fig. 1 and S3) corroborate this observation, in that the biotransformed GOs consisted of more wrinkled and randomly stacked sheets, which are common for reduced GOs[19]. The AFM height and size profiles (Fig. 1 and S7) show that the thickness and lateral size of the GO nanosheets increased upon biotransformation, particularly for Gamble-GO, which is likely due to an increase in the van der Waals forces and hydrophobicity following GO reduction, resulting in a greater tendency for nanosheet aggregation[20].

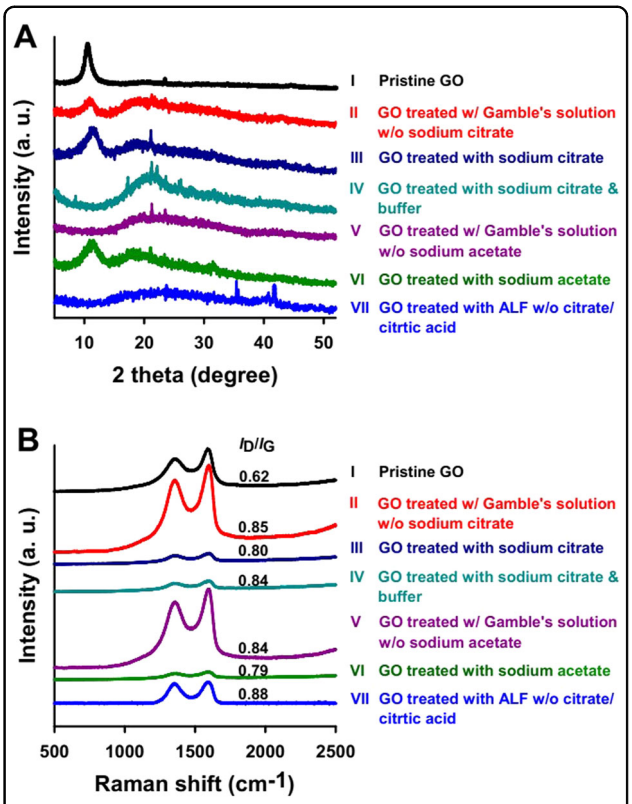

Fig. 2 Comparison of the X-ray diffraction (XRD) patterns (**a**) and Raman spectra (**b**) of pristine GO (I) and the GOs treated with different components of the simulated human lung fluids (II–VII), showing that the organic acids present in the simulated human lung fluids were the primary constituents responsible for the bioreduction of GO. XRD patterns: the incomplete reduction of GO in the absence of sodium citrate (II) indicates the important role of citrate, whereas the fact that significant reduction of GO by citrate was not observed at acidic pH (III) but was observed at neutral pH (IV) indicates that the effectiveness of citrate is pH dependent. In comparison, significant GO reduction occurred in the absence of sodium acetate (V), indicating that even though acetate was capable of reducing GO (VI), its overall contribution was small. The significant reduction of GO by ALF in the absence of both citrate and citric acid (VII) indicates that other organic acids also made substantial contributions to GO reduction. Raman spectra: the increase in the I_D/I_G ratio (indicative of the formation of new small-sized graphitic domains) for the GOs treated with different lung fluid components is generally consistent with the roles of the organic acids determined from the XRD patterns

Organic acids in lung fluids are the primary components inducing the GO transformation

The biodegradation of GO materials by proteins, enzymes, and macrophages was previously reported[21–25]. Even though the specific mechanisms were not discussed,

it is reasonable to assume that GO materials are reactive toward biological species. Both Gamble's solution and ALF contain a mixture of organic acids and their salts, as well as inorganic salts, whereas the two lung fluids differ in the types and concentrations of individual components (Table S1). The organic acids and their salts (e.g., sodium acetate and sodium citrate in Gamble's solution) are redox active[26,27], and are likely the primary components responsible for GO reduction. However, the inorganic salts, in particular, the pH buffer components, may affect the redox potential[28] and consequently also influence GO reduction. To identify the primary components of the lung fluids that were responsible for GO reduction, we conducted a series of experiments involving individual components or an assortment of lung fluid components. The XRD patterns were used as the primary evidence in this set of experiments, as the decrease in the intensity of the (002) peak of GO (~10°) and the increase in the characteristic peak of reduced GO (~20°) provide direct evidence of GO reduction[15].

We first examined the contributions of sodium citrate and sodium acetate to the transformation of GO by Gamble's solution. In the absence of sodium citrate (Fig. 2, XRD pattern II), the reduction of GO was incomplete (the peak intensity at ~10° decreased but did not disappear, as was the case when GO was treated with the complete Gamble's solution, Fig. 1a), indicating the important role of citrate in GO reduction. Interestingly, treating GO with citrate alone (pH of ~3.8) did not result in the significant reduction of GO (pattern III), whereas when GO was treated with citrate in pH buffer (pH of ~7.4), the peak at ~10° essentially disappeared (pattern IV). Based on the pK_a values of citrate (pK_{a1} = 3.13, pK_{a2} = 4.76, and pK_{a3} = 6.40), the primary species in Gamble's solution (pH ~ 7.4) is $C_6H_5O_7^{3-}$. This species can form dicarboxy acetone and release an electron (eq. 1)[29], leading to GO reduction (note that without pH buffer, the release of H^+ hindered the reaction):

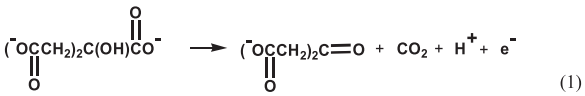

(1)

It is noteworthy that significant reduction of GO occurred even when sodium acetate was removed from Gamble's solution (pattern V), indicating that even though acetate is capable of reducing GO (pattern VI), its overall contribution is small compared with that of citrate.

The important role of citrate demonstrated above was consistent with the greater extent of GO reduction in ALF than in Gamble's solution. The concentration of citrate in

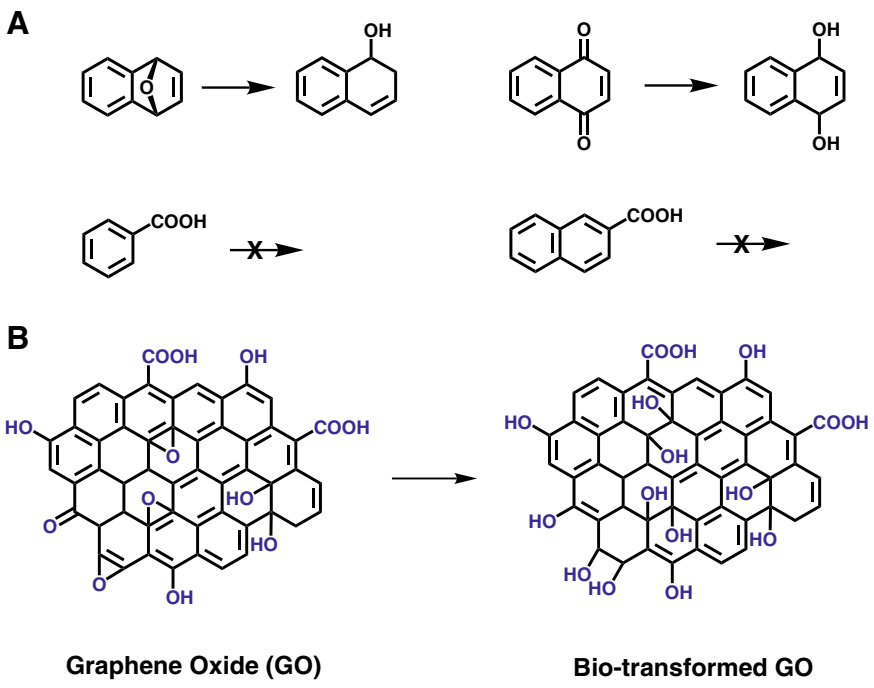

Fig. 3 Two model compounds—1,4-epoxynaphthalene (selected to represent the epoxy-containing domain of GO) and 1,4-naphthoquinone (representing the carbonyl-containing domain)—can be effectively reduced in either Gamble's solution or sodium citrate in buffer (pH 7.4), whereas benzoic acid and 2-naphthoic acid (representing the carboxyl-containing domain) cannot be transformed (a). These results indicate that the bioreduction of GO in the simulated human lung fluids likely involves the ring-opening of epoxy groups (to form hydroxyl groups) and the transformation of carbonyl groups to hydroxyl groups. A schematic illustration of the mechanisms of GO biotransformation in the simulated human lung fluids (**b**) is proposed based on the reactions of these model compounds

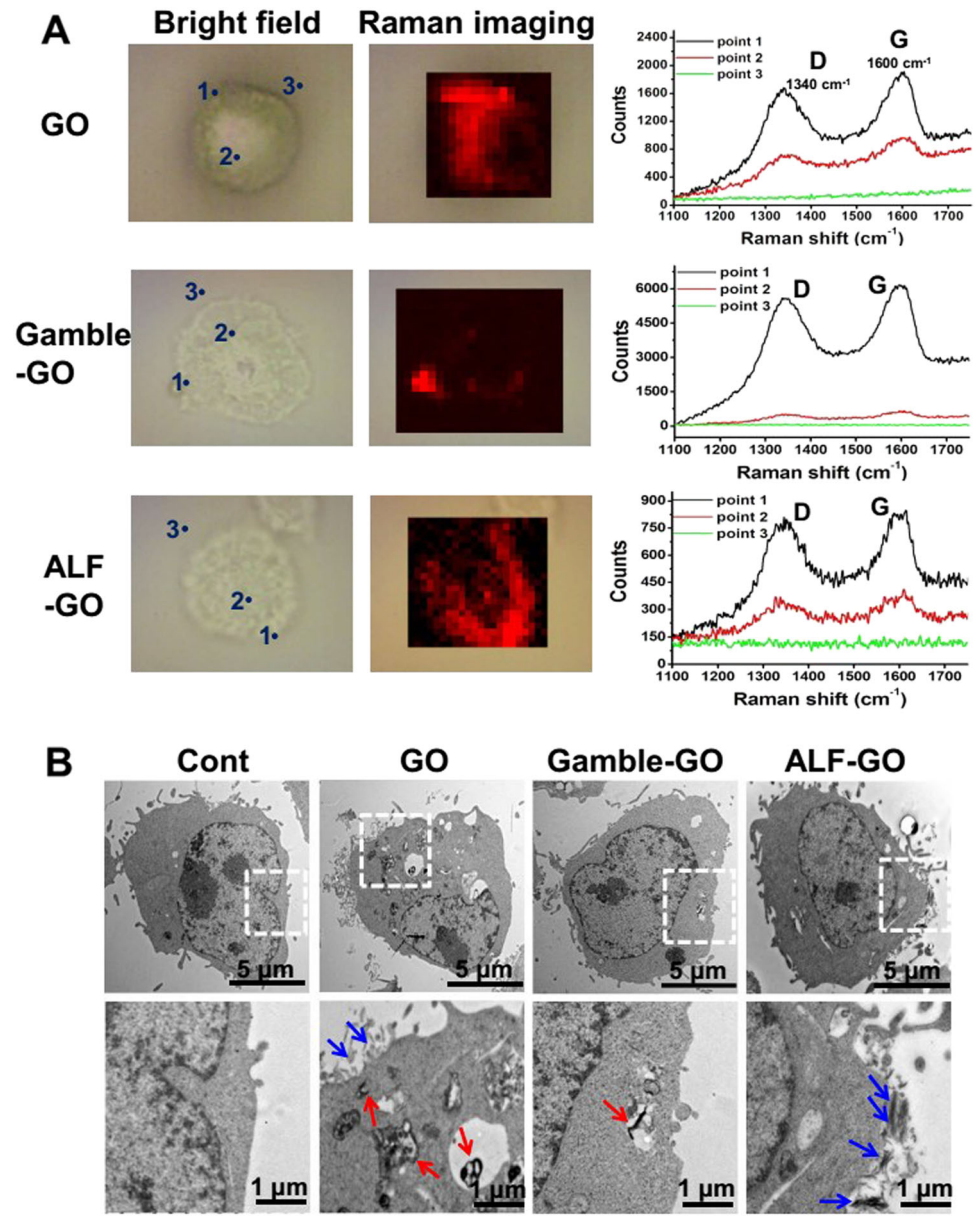

Fig. 4 Interactions of pristine GO, GO treated with Gamble's solution (Gamble-GO), and GO treated with artificial lysosomal fluid (ALF-GO) with J774A.1 cells, showing reduced interactions with the plasma membrane for Gamble-GO and the adhesion of ALF-GO to the plasma membrane without cellular uptake. a Raman mapping of the J774A.1 cells upon exposure to 5 μg/mL GO, Gamble-GO, and ALF-GO for 24 h. The Raman image is overlapped with its corresponding bright-field image. The red area in the Raman images represents the signal of different GO nanomaterials. A typical Raman spectrum was acquired from three target points. Point 1 and Point 2 were located on the boundary and inside the cell, respectively, and Point 3 was randomly chosen outside the cell. **b** High-resolution TEM images (original magnification, ×10,000) of cells treated with 5 μg/mL GO for 24 h. Representative associations of the nanomaterials with the cell membrane (blue arrows) and inside phagosomes (red arrows) are indicated in the enlarged images (below) from the dashed-line squares

ALF (0.077 g/L sodium citrate and 20.8 g/L citric acid) was much higher than that in Gamble's solution, making ALF a more potent reductant. Strikingly, significant reduction of GO was observed when both citrate and citric acid were removed from ALF (pattern VII). Thus, it appears that the other organic acids (e.g., lactate and tartrate) also contributed to the significant reduction of GO by ALF. Overall, it appeared that the organic acids in Gamble's solution and ALF were the primary components responsible for the transformation of GO.

GO reduction is mainly due to the conversion of epoxy and carbonyl groups to phenolic groups

The combined evidence of the FT-IR spectra (Fig. 1c) and XPS data (Table 1 and Figure S1) indicated that the biotransformation of GO was mainly due to the conversion of epoxy and carbonyl groups to phenolic groups. To understand the underlying mechanisms controlling the loss/conversion of the GO surface functional groups when treated with Gamble's solution and ALF, we examined the reactions of 1,4-epoxynaphthalene, 1,4-naphthoquinone, benzoic acid, and 2-naphthoic acid—four small organic molecules representing the epoxide, carbonyl, and carboxyl-containing fragments of GO—with Gamble's solution and citrate (the key component of Gamble's solution and ALF responsible for GO reduction). The detected reaction products (Figure S5) showed that both Gamble's solution and citrate in pH buffer can convert 1,4-epoxynaphthalene to 1,2-dihydro-1-naphthol and 1,4-naphthoquinone to 1,4-dihydro-1,4-naphthalenediol (Fig. 3a), corroborating the occurrence of a ring-opening reaction of epoxy groups to form phenolic groups and the conversion of carbonyl groups to phenolic groups. In comparison, neither Gamble's solution nor citrate in pH buffer facilitated the reduction of benzoic acid and 2-naphthoic acid (Fig. 3a). While the reactions shown in Fig. 3a may not sufficiently capture the complex conversion/removal of the O-containing functionalities of GO by the lung fluids, the reduction mechanisms illustrated herein are generally consistent with the overall observed loss of epoxy groups and carbonyl groups. A pictorial illustration of the biotransformation pathways of GO induced by the two lung fluids is shown in Fig. 3b. It is necessary to note that the XPS data show that the concentrations of surface carboxyl groups of GO increased following treatment with the lung fluids, particularly when GO was treated with ALF. Since none of the reactions in Fig. 3a indicate the formation of carboxyl groups, one possible explanation for the increased concentration of carboxyl groups is the adsorption of organic acids to GO[30]. Another possible mechanism for the increase in the carboxyl group content is the hydrolysis of acid anhydrides on GO[31].

Biotransformation substantially alters the interaction of GO with macrophages

The reactivity at the nanobiointerface, which consequently dictates the cytocompatibility/biocompatibility of nanomaterials, is essentially determined by the physicochemical properties of the materials. To this end, the interaction of the biotransformed GO materials with macrophages and their fate was assessed. To avoid high-dose exposure that may not realistically occur and would incur extensive cell death, we used sublethal concentrations of GO materials (≤20 μg/mL) in treating J774A.1 cells[6,32].

The localization of the GO sheets was detected via confocal micro-Raman spectroscopy[33]. Fig. 4a illustrates the merged images of the Raman maps with the corresponding bright-field morphologies of the J774A.1 cells treated with pristine GO, Gamble-GO, and ALF-GO at 5 μg/mL for 24 h. For each treatment, three points were examined by Raman spectroscopy, where Points 1 and 2 are located near the boundary of the cell membrane and inside the cells, respectively, and Point 3 is located outside the cells (Fig. 4a). Consistent with previous observations[9,34], a canonical Raman spectrum was obtained at Point 1 (i.e., at the border of the cell membrane) for the cells treated with pristine GO, with the representative graphitic lattice band (G band) observed at 1600 cm^{-1} and the disorder band (D band) observed at 1340 cm^{-1}, and a weaker Raman intensity was found at Point 2 (Fig. 4a). This observation revealed the active interaction between pristine GO and macrophages. For the ALF-GO-treated cells, a seemingly stronger Raman intensity was obtained at Point 1 compared to that at Point 1 of the pristine GO-treated cells (Fig. 4a), indicating stronger interaction between ALF-GO and the cell membrane. By contrast, much weaker Raman signals were obtained at Point 1 and Point 2 for the Gamble-GO-treated cells, suggesting the weak interaction between Gamble-GO and macrophages. Here, Point 3 was used a reference site (outside the cell), as nearly no Raman signal was obtained for all treatments (Fig. 4a).

Since confocal micro-Raman spectroscopy was unable to define the morphology of the GO materials and discern their precise locations (either adsorbed on the plasma membrane or underneath the plasma membrane), we further carried out TEM analysis to visualize the localization of GO (Fig. 4b). For the cells treated with pristine GO, GO sheets were observed both on the plasma membrane (with some sheets parallel to the plasma membrane, as indicated by blue arrows) and inside the cytoplasm in membrane-bound structures, which are presumably phagosomes (denoted by red arrows), in agreement with the results of previous studies[6,9,34]. Unlike pristine GO, very little Gamble-GO was observed inside the cytoplasm and on the plasma membrane in the J774A.1 macrophages (Fig. 4b), indicating the rather weak association of Gamble-GO with macrophages. In stark contrast, ALF-GO displayed a distinct fate in macrophages with no sign of being phagocytosed, as no phagosomes with ALF-GO could be found in the J774A.1 cells (Fig. 4b). Instead, ALF-GO aggregated into clusters and adhered to the plasma membrane without undergoing phagocytosis, leading to the formation of fairly thick GO sheet complexes attached to the plasma membrane (denoted by blue arrows in Fig. 4b), similar to

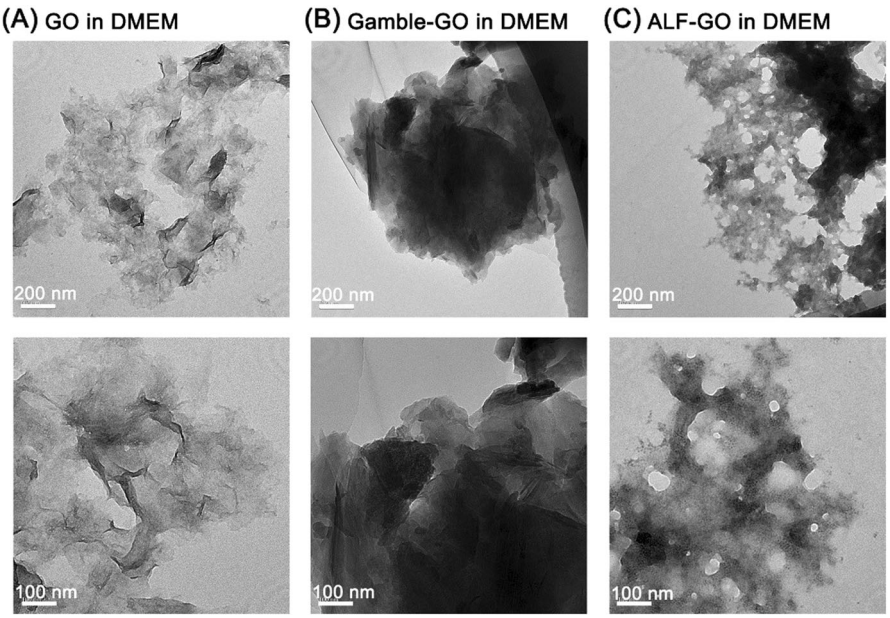

Fig. 5 Transmission electron microscopy (TEM) images of pristine GO (**a**), Gamble-GO (**b**), and ALF-GO (**c**) incubated in Dulbecco's modified Eagle's medium (DMEM) containing 10% fetal bovine serum (FBS) for 24 h showing that the three materials exhibited different manners of aggregation in the medium. Particularly, Gamble-GO aggregated in a layer-to-layer manner, whereas ALF-GO favored the formation of edge-to-edge aggregates

our recent observation that larger-sized GO nanosheets exhibited stronger associations with the plasma membrane, resulting in reduced phagocytosis[9].

The strikingly different interactions with macrophages among pristine GO, Gamble-GO, and ALF-GO appeared to be related to changes in the physicochemical properties of GO due to bioreduction. The biotransformation significantly increased the hydrophobicity of GO through the elimination of surface O-containing functional groups, thereby increasing the tendency of the nanosheets to aggregate for both Gamble-GO and ALF-GO[35,36]. Nonetheless, owing to its high concentration of surface carboxyl groups, ALF-GO was likely to form large sheet-like aggregates via the cation-bridging mechanism[37,38], wherein divalent cations (e.g., Ca^{2+}) cross-linked the carboxyl groups of neighboring nanosheets. In comparison, Gamble-GO tended to aggregate in a layer-to-layer configuration, as the loss of O-containing functional groups decreased the extent of cation-induced cross-linking of individual nanosheets and caused the van der Waals forces and π–π interactions to be more dominant[37–39]. The differences in the aggregation properties between Gamble-GO and ALF-GO were verified by TEM analysis of the two materials incubated in DMEM with 10% FBS for 24 h (Fig. 5). Consequently, the stacked, chunk-like aggregates of Gamble-GO precipitated easily, reducing the likelihood of their association with the plasma membrane. In comparison, the large-area aggregates of ALF-GO were susceptible to plasma membrane adsorption, wherein the contact between the large, flat side with the plasma membrane provoked the shape spreading of the macrophages without performing phagocytosis[9,40,41], as reflected by the elevated average cellular size of the ALF-GO-treated cells (Fig. 4). The inhibited endocytosis of the bioreduced GOs may lead to potentially long-term side effects and diverse toxicities at the accumulation sites.

To further confirm the differential interactions with macrophages of GO, Gamble-GO, and ALF-GO, which are affected by the specific aggregation properties of these materials, we conducted animal experiments. The TEM images of bronchoalveolar lavage fluids collected from mice exposed to GO for 3 h (Figure S6) clearly show the presence of aggregates in both layer-to-layer and edge-to-edge configurations, corroborating our results from the cell experiments. Furthermore, H&E staining showed remarkably different interactions of the cells with GO and the two biotransformed GOs (Figure S7). For example, after 24 h of exposure, GO was mostly cleared, and only a very small amount of GO nanosheets was observed. In contrast, GO aggregates were easily visualized in the lungs of mice exposed to the two biotransformed GOs, indicating that biotransformation impaired the clearance process. Consistent with the cell experiments, Gamble-GO tended to form stacked aggregates, whereas ALF-GO existed mainly as large-area aggregates.

Overall, these results indicated that biotransformation fundamentally changed the reactivity of GO toward

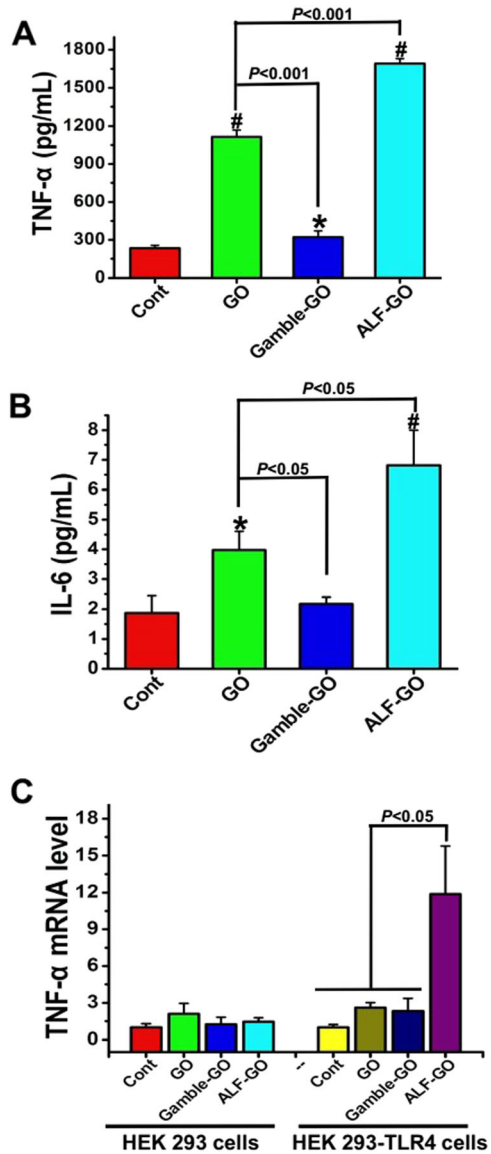

Fig. 6 Proinflammatory responses elicited by pristine GO, GO treated with Gamble's solution (Gamble-GO), and GO treated with artificial lysosomal fluid (ALF-GO), showing that the biotransformations in the different lung fluids resulted in varied capabilities of the GO materials to provoke TNF-α production. a, **b** Levels of secreted cytokines TNF-α and IL-6 in the cell culture supernatants when J774A.1 cells were treated with 20 μg/mL GO for 24 h ($n = 5$). **c** TNF-α expression levels in HEK293 cells and HEK293-TLR4 cells in response to different GO materials (at 20 μg/mL) for 12 h ($n = 5$). Asterisk (*): $P < 0.05$; pound sign (#): $P < 0.001$ compared to the control (cells receiving no GO treatment)

macrophages and impeded the endocytosis of GO nanosheets by macrophages. Meanwhile, remarkable differences were found between Gamble-GO and ALF-GO, as Gamble-GO was less frequently recognized and phagocytosed than pristine GO, and ALF-GO tended to adhere to the plasma membrane without being internalized. Even though two different mechanisms were responsible for the inhibited endocytosis of Gamble-GO and ALF-GO, both mechanisms result in the impaired clearance of GO from the body, leading to potentially long-term side effects and diverse toxicities at the accumulation sites.

ALF-GO and Gamble-GO differentially activate macrophages into a proinflammatory state

The distinctly different bioactivities of Gamble-GO and ALF-GO encouraged us to conceive of differential activation of macrophages by these biotransformed GOs. Therefore, macrophagic activation toward proinflammatory phenotypes was evaluated by assessing the proinflammatory cytokines secreted into the cell culture medium. Interestingly, the two biotransformed GOs exhibited different capabilities to provoke TNF-α production. In analogy to previous studies[9,33], the treatment of J774A.1 cells with pristine GO (20 μg/mL for 24 h) markedly stimulated TNF-α production by nearly fivefold compared to that in untreated cells (Fig. 6a, $P < 0.001$). In comparison, Gamble-GO showed a much weaker capability to elevate TNF-α secretion than pristine GO, giving a TNF-α level comparable to that of untreated cells (Fig. 6a), in line with the weak interaction between Gamble-GO and macrophages, as illustrated in Fig. 5b. Consistent with the strong interaction with macrophages, ALF-GO resulted in a 52% further increase in the TNF-α level in J774A.1 cells compared with that induced by pristine GO (Fig. 6a, $P < 0.001$), indicative of enhanced inflammatory responses in the J774A.1 cells. This finding highlighted the close attachment of ALF-GO aggregates to the plasma membrane, which could readily trigger macrophagic activation. To substantiate the differential inflammatory reactions of macrophages by different GOs, another proinflammatory cytokine, IL-6, was assayed. As shown in Fig. 6b, a similar trend in IL-6 production to that of TNF-α production in J774A.1 cells was observed upon treatment with pristine GO, Gamble-GO, and ALF-GO ($P < 0.05$). On the basis of these results, we assumed that the biotransformation-induced changes in the GO physicochemical properties play a critical role in its interaction with macrophages.

To corroborate this hypothesis, we used a cell model of HEK293/TLR4 cells, which harbored artificial TLR4 expression in HEK293 cells, to further investigate the role of TLR4 signaling in regulating the inflammatory responses elicited by GO materials[9]. Our previous studies demonstrated that membrane TLR4 essentially senses GO sheets on the plasma membrane and consequentially activates macrophages to secrete proinflammatory cytokines through NF-κB signaling[9,33]. Thus, this cell model is ideal for testing the capability of invading particles to activate macrophages. Similar to previous observations[9],

TNF-α production was not induced in the original HEK293 cells without exotic TLR4 upon treatment with the GO materials (Fig. 6c). However, all GO materials triggered TNF-α expression in the HEK293/TLR4 cells but to different extents (Fig. 6c, $P < 0.05$). Specifically, pristine GO and Gamble-GO similarly increased TNF-α expression by ~2-fold relative to that in the untreated cells (Fig. 6c, $P < 0.05$). By contrast, ALF-GO considerably enforced TNF-α expression by more than 10-fold compared to that in the untreated cells (Fig. 6c, $P < 0.05$), signifying the potent capability of ALF-GO to activate macrophages by acting on TLR4 signaling.

These data together revealed a previously unrecognized changeover, that is, in contrast to pristine GO, the two biotransformed GOs dramatically escaped clearance by macrophages. Meanwhile, we deciphered the molecular mechanisms responsible for the differential bioactivities of Gamble-GO and ALF-GO toward macrophages: the loss of association with the plasma membrane for Gamble-GO vs. enhanced adhesion to the plasma membrane for ALF-GO. Furthermore, the mechanical stress on the plasma membrane induced by ALF-GO caused the macrophages to produce proinflammatory phenotypes through TLR4 signaling.

Conclusion

In conclusion, GO materials underwent biotransformation in simulated lung fluids, which significantly impaired their clearance by macrophages. Notably, the biotransformation of GO in different biological settings resulted in markedly distinct effects on the physicochemical properties of GO, which consequently affected its bioactivity at the nanobiointerface. Overall, the findings reveal the remarkable impact that in vivo biotransformation of GO has on its properties and biosafety, and emphasize the need to consider the biotransformation-associated effects of nanomaterials in biomedical applications.

Acknowledgements

This project was supported by the national "973" program (Grant 2014CB932000) and the National Natural Science Foundation of China (Grants 21425729, 21425731, 21637004, and 21607157).

Author details

[1]College of Environmental Science and Engineering, Ministry of Education Key Laboratory of Pollution Processes and Environmental Criteria, Tianjin Key Laboratory of Environmental Remediation and Pollution Control, Nankai University, 300350 Tianjin, China. [2]State Key Laboratory of Environmental Chemistry and Ecotoxicology, Research Center for Eco-Environmental Sciences, Chinese Academy of Sciences, 100085 Beijing, China. [3]Key Laboratory of High Magnetic Field and Ion Beam Physical Biology, Hefei Institutes of Physical Science, Anhui Province Key Laboratory of Environmental Toxicology and Pollution Control Technology, Chinese Academy of Sciences, 230031 Hefei, Anhui, China. [4]Division of Nanomedicine, Department of Medicine, University of California, Los Angeles, CA 90095, USA. [5]University of Chinese Academy of Sciences, 100049 Beijing, China

Conflict of interest

The authors declare that they have no conflict of interest.

Publisher's note

Springer Nature remains neutral with regard to jurisdictional claims in published maps and institutional affiliations.

Supplementary information is available for this paper at https://doi.org/10.1038/s41427-018-0039-0.

Received: 17 November 2017 Revised: 13 March 2018 Accepted: 19 March 2018.
Published online: 15 May 2018

References

1. Dostert, C. et al. Innate immune activation through Nalp3 inflammasome sensing of asbestos and silica. *Science* **320**, 674–677 (2008).
2. Ghebre, Y. T. & Raghu, G. Idiopathic pulmonary fibrosis: novel concepts of proton pump inhibitors as antifibrotic drugs. *Am. J. Resp. Crit. Care Med.* **193**, 1345–1352 (2016).
3. Zhang, L., Xia, J., Zhao, Q., Liu, L. & Zhang, Z. Functional graphene oxide as a nanocarrier for controlled loading and targeted delivery of mixed anticancer drugs. *Small* **6**, 537–544 (2010).
4. Hong, H. et al. In vivo targeting and imaging of tumor vasculature with radiolabeled, antibody-conjugated nano-graphene. *ACS Nano* **6**, 2361–2370 (2012).
5. Li, Z. et al. Graphene oxide/Ag nanoparticles cooperated with simvastatin as a high sensitive X-ray computed tomography imaging agent for diagnosis of renal dysfunctions. *Adv. Healthc. Mater.* **6**, 1700413 (2017).
6. Zhu, J. et al. Graphene oxide induced perturbation to plasma membrane and cytoskeletal meshwork sensitize cancer cells to chemotherapeutic agents. *ACS Nano* **11**, 2637–2651 (2017).
7. Yin, T. et al. In vivo high-efficiency targeted photodynamic therapy of ultrasmall Fe_3O_4@polymer-NPO/PEG-Glc@Ce_6 nanoprobes based on small size effect. *NPG Asia Mater.* **9**, e383 (2017).
8. Jin, Y. et al. Biodegradable, multifunctional DNAzyme nanoflowers for enhanced cancer therapy. *NPG Asia Mater.* **9**, e365 (2017).
9. Ma, J. et al. Crucial role of lateral size for graphene oxide in activating macrophages and stimulating pro-inflammatory responses in cells and animals. *ACS Nano* **9**, 10498–10515 (2015).
10. Ma, J. et al. Carbon nanotubes stimulate synovial inflammation by inducing systemic pro-inflammatory cytokines. *Nanoscale* **8**, 18070–18086 (2016).
11. Mühlfeld, C. et al. Interactions of nanoparticles with pulmonary structures and cellular responses. *Am. J. Physiol. Lung Cell. Mol. Physiol.* **294**, 817–829 (2008).
12. Hu, Q., Bai, X., Hu, G. & Zuo, Y. Y. Unveiling the molecular structure of pulmonary surfactant corona on nanoparticles. *ACS Nano* **11**, 6832–6842 (2017).
13. Chua, C. & Pumera, M. Chemical reduction of graphene oxide: a synthetic chemistry viewpoint. *Chem. Soc. Rev.* **43**, 291–312 (2014).
14. Dong, L. et al. Tuning magnetic property and autophagic response for self-assembled Ni-Co alloy nanocrystals. *Adv. Funct. Mater.* **23**, 5930–5940 (2013).
15. Fan, Z. et al. Facile synthesis of graphene nanosheets via Fe reduction of exfoliated graphite oxide. *ACS Nano* **5**, 191–198 (2011).
16. Shin, H.-J. et al. Efficient reduction of graphite oxide by sodium borohydride and its effect on electrical conductance. *Adv. Funct. Mater.* **19**, 1987–1992 (2009).
17. Stankovich, S. et al. Synthesis of graphene-based nanosheets *via* chemical reduction of exfoliated graphite oxide. *Carbon NY* **45**, 1558–1565 (2007).
18. Li, M., Cushing, S. K., Zhou, X., Guo, S. & Wu, N. Fingerprinting photoluminescence of functional groups in graphene oxide. *J. Mater. Chem.* **22**, 23374–23379 (2012).
19. Gómez-Navarro, C. et al. Atomic structure of reduced graphene oxide. *Nano Lett.* **10**, 1144–1148 (2010).
20. Liu, S. et al. Antibacterial activity of graphite, graphite oxide, graphene oxide, and reduced graphene oxide: membrane and oxidative stress. *ACS Nano* **5**, 6971–6980 (2011).
21. Kurapati, R. et al. Dispersibility-dependent biodegradation of graphene oxide by myeloperoxidase. *Small* **11**, 3985–3994 (2015).

22. Kotchey, G. P. et al. The enzymatic oxidation of graphene oxide. *ACS Nano* **5**, 2098–2108 (2011).
23. Hu, X., Li, D. & Mu, L. Biotransformation of graphene oxide nanosheets in blood plasma affects their interactions with cells. *Environ. Sci.* **4**, 1569–1578 (2017).
24. Girish, C. M., Sasidharan, A., Gowd, G. S., Nair, S. & Koyakutty, M. Confocal raman imaging study showing macrophage mediated biodegradation of graphene in vivo. *Adv. Healthc. Mater.* **2**, 1489–1500 (2013).
25. Bhattacharya, K. et al. Biological interactions of carbon-based nanomaterials: from coronation to degradation. *Nanomedicine* **12**, 333–351 (2016).
26. Zhang, Z. et al. Sodium citrate: a universal reducing agent for reduction/ decoration of graphene oxide with Au nanoparticles. *Nano Res.* **4**, 599–611 (2011).
27. Agharkar, M., Kochrekar, S., Hidouri, S. & Azeez, M. A. Trends in green reduction of graphene oxides, issues and challenges: a review. *Mater. Res. Bull.* **59**, 323–328 (2014).
28. Ji, X. et al. Size control of gold nanocrystals in citrate reduction: the third role of citrate. *J. Am. Chem. Soc.* **129**, 13939–13948 (2007).
29. Kumar, S., Gandhi, K. S. & Kumar, R. Modeling of formation of gold nanoparticles by citrate method. *Ind. Eng. Chem. Res.* **46**, 3128–3136 (2007).
30. Zhang, J. et al. Reduction of graphene oxide via L-ascorbic acid. *Chem. Commun.* **46**, 1112–1114 (2010).
31. Clayden, J., Greeves, N. & Warren, S. *Organic Chemistry*. 2 ed., (OUP, Oxford, 2012).
32. Chen, Y. et al. Genome-wide DNA methylation variations upon exposure to engineered nanomaterials and their implications in nanosafety assessment. *Adv. Mater.* **29**, 1604580 (2017).
33. Qu, G. et al. Graphene oxide induces toll-like receptor 4 (TLR4)-dependent necrosis in macrophages. *ACS Nano* **7**, 5732–5745 (2013).
34. Xu, M. et al. Improved in vitro and in vivo biocompatibility of graphene oxide through surface modification: poly(acrylic acid)-functionalization is superior to PEGylation. *ACS Nano* **10**, 3267–3281 (2016).
35. Chowdhury, I., Mansukhani, N. D., Guiney, L. M., Hersam, M. C. & Bouchard, D. Aggregation and stability of reduced graphene oxide: complex roles of divalent cations, pH, and natural organic matter. *Environ. Sci. Technol.* **49**, 10886–10893 (2015).
36. Qi, Y., Xia, T., Li, Y., Duan, L. & Chen, W. Colloidal stability of reduced graphene oxide materials prepared using different reducing agents. *Environ. Sci.* **3**, 1062–1071 (2016).
37. Park, S. et al. Graphene oxide papers modified by divalent ions-enhancing mechanical properties via chemical cross-linking. *ACS Nano* **2**, 572–578 (2008).
38. Wu, L. et al. Aggregation kinetics of graphene oxides in aqueous solutions: experiments, mechanisms, and modeling. *Langmuir* **29**, 15174–15181 (2013).
39. Cote, L. J., Kim, F. & Huang, J. Langmuir-Blodgett assembly of graphite oxide single layers. *J. Am. Chem. Soc.* **131**, 1043–1049 (2009).
40. Champion, J. A. & Mitragotri, S. Role of target geometry in phagocytosis. *Proc. Natl Acad. Sci. USA* **103**, 4930–4934 (2006).
41. Doshi, N. & Mitragotri, S. Macrophages recognize size and shape of their targets. *PLoS ONE* **5**, e10051 (2010).